The Journal of Chemical Physics ARTICLE scitation.org/journal/jcp

Microsecond dynamics in proteins by two-dimensional ESR: Predictions

Cite as: J. Chem. Phys. 152, 214112 (2020); doi: 10.1063/5.0008094
Submitted: 19 March 2020 • Accepted: 14 April 2020 •
Published Online: 4 June 2020

Pranav Gupta, Zhichun Liang, and Jack H. Freed[a)]

AFFILIATIONS

Department of Chemistry and Chemical Biology, National Biomedical Center for Advanced ESR Technology, Cornell University, Ithaca, New York 14853, USA

[a)]Author to whom correspondence should be addressed: jhf3@cornell.edu

ABSTRACT

Two-dimensional electron–electron double resonance (2D-ELDOR) provides extensive insight into molecular motions. Recent developments permitting experiments at higher frequencies (95 GHz) provide molecular orientational resolution, enabling a clearer description of the nature of the motions. In this work, simulations are provided for the example of domain motions within proteins that are themselves slowly tumbling in solution. These show the nature of the exchange cross-peaks that are predicted to develop in real time from such domain motions. However, we find that the existing theoretical methods for computing 2D-ELDOR experiments over a wide motional range begin to fail seriously when applied to very slow motions characteristic of proteins in solution. One reason is the failure to obtain accurate eigenvectors and eigenvalues of the complex symmetric stochastic Liouville matrices describing the experiment when computed by the efficient Lanczos algorithm in the range of very slow motion. Another, perhaps more serious, issue is that these matrices are "non-normal," such that for the very slow motional range even rigorous diagonalization algorithms do not yield the correct eigenvalues and eigenvectors. We have employed algorithms that overcome both these issues and lead to valid 2D-ELDOR predictions even for motions approaching the rigid limit. They are utilized to describe the development of cross-peaks in 2D-ELDOR at 95 GHz for a particular case of domain motion.

I. INTRODUCTION

Spin-label ESR spectroscopy has been widely demonstrated to be a powerful tool in investigating the local dynamics and structure of complex fluids, model and biological membranes, polymers, proteins, and protein complexes.[1–8] Two separate strategies for further extending the capabilities of ESR in studying molecular dynamics have emerged: multi-frequency ESR and two-dimensional electron–electron double resonance (2D-ELDOR). Multi-frequency cw ESR can cover a large range of ESR frequencies—for example, a 9–240 GHz study on the motional dynamics in the protein T4 lysozyme.[9] This approach sensitively detects and discriminates motions occurring on different time scales. Such studies have been greatly enhanced by developments extending ESR to high magnetic fields and frequencies, which provide greatly improved orientational resolution as well as better insight into faster motional dynamics.[1,4,10–13] Thus, multi-frequency ESR experiments can unravel the details of dynamical modes of complex systems.[1,4,9,11,12] 2D-ELDOR studies disentangle the homogeneous broadening, which provides insight into molecular motions, from the inhomogeneous broadening, which relates to local structure and ordering.[1,14–19] Furthermore, they supply cross-peaks that directly report on the dynamics of labeled molecules (e.g., biomolecules), which can range from tens of nanoseconds to tens of microseconds. This range is limited, respectively, by spectrometer resolution and by the sample T_1.

Technological developments[10,14,19–22] have begun to enable performing 2D-ELDOR on complex fluids at high frequency (95 GHz), thus combining the virtues of 2D-ELDOR with those of multi-frequency ESR. Given these developments, we describe in this paper theoretical simulations which predict how 95 GHz 2D-ELDOR can be used to detect internal dynamic modes of motion in labeled proteins occurring in the microsecond range. This is challenging not only experimentally but also theoretically. The very slow overall tumbling motions and the large orientational resolution both place considerable demands on the existing theoretical software.[23,24] In fact, these Lanczos-based methods for diagonalizing the appropriate complex symmetric stochastic Liouville matrices are no longer

stable due to the well-known loss of orthogonality of the Lanczos vectors[23,25,26] as well as the fact that they become severely "non-normal."[27,28] Despite these issues, we have found over the years that for cw (continuous wave) ESR, it was possible to use Lanczos-based methods even for very slow motions at 95 GHz and higher frequencies, in part because it was not necessary to diagonalize the tridiagonal Lanczos matrices, as described in detail elsewhere.[23,25] However, in the existing algorithm for 2D-ELDOR,[29] it is necessary to obtain and utilize accurate eigenvalues and eigenvectors, which leads to poor results at very slow motions and high ESR frequencies. So, we needed to develop another approach. Yet, we feel it is important to obtain initial predictions of the possibilities before engaging in such challenging experiments. Thus, we report on our latest improvements in computational analysis compared to past versions, since they offer greater stability in the very slow-motional regime. Then, we are able to simulate experimental 2D-ELDOR at ultra-slow motions, all the way to the rigid limit. We have also generated slow-motional 2D-ELDOR spectra corresponding to a prospective biophysical application, namely, conformational exchange in biomolecules, such as that occurring in the G-protein coupled receptor rhodopsin.[30,31]

It has been long appreciated that nanosecond-to-microsecond local dynamics play an essential role in the biological functions of proteins.[32–37] Local protein dynamics determine enzymatic function,[32,38] enable signal propagation,[35,39] and confer the ability to bind ligands and drugs.[33,40] With the advent of routine microsecond-long molecular dynamic simulations, enzymatic mechanisms and conformational signaling processes are increasingly being proposed with atomistic detail.[35–37,41–44] However, there remains a paucity of experimental approaches capable of characterizing the relevant dynamics of large complex systems, such as membrane proteins.[34,45–49] Nonetheless, it is clear that to approach processes such as transmembrane signaling by receptors, local dynamics, and their ability to propagate must be understood.[34,35,37–39,42,44,46–49] 2D-ELDOR spectroscopy of spin-labeled proteins offers such a tool. With a firm theoretical framework in place to interpret spin dynamics in terms of molecular structure and motion, underlying physical principles of protein function relevant to drug design have the potential to be revealed.

II. 2D-ELDOR: AN OVERVIEW

The analysis of ESR experiments requires us to consider both the rotational and the spin degrees of freedom of the electron spin probe under consideration. The following Stochastic Liouville Equation (SLE)[23,29,50] is an accurate representation of this dynamics:

$$\frac{\partial \rho(\Omega,t)}{\partial t} = (-i\mathcal{H}^{\times} - \Gamma(\Omega))(\rho(\Omega,t) - \rho_{eq}(\Omega)) := -\mathcal{L}(\rho(\Omega,t) - \rho_{eq}(\Omega)). \quad (1)$$

Here ρ is the time (t)- and orientation (Ω)-dependent electron spin density matrix with an equilibrium value $\rho_{eq}(\Omega)$, and $\mathcal{H}^{\times}$ is the electron spin Hamiltonian superoperator ($\mathcal{H}^{\times}\rho$ is defined as $[\mathcal{H},\rho]$). Γ is the classical, orientation-dependent relaxation superoperator, of which rotational diffusion is the major component. Also, $\mathcal{L}$ is known as the *Liouville superoperator*. As suggested by the equation above, $\mathcal{L}$ describes the combined effects of the electron spin Hamiltonian superoperator and the relaxation superoperator Γ.

In a two-dimensional ESR experiment such as 2D-ELDOR, we employ high-power microwave pulses in order to excite the widest possible bandwidth, and yet these pulses are typically much shorter than the relaxation time scales of the electron spins. In these experiments, it is true that the electron spin coherence order, p^S, does not change between successive microwave pulses.[29] This simplifies the computation of the 2D-ELDOR spectrum, and allows us to treat the microwave pulses as just leading to changes in the coherence order, so that between successive pulses when the microwave field is absent, we just need to consider the effects of $\mathcal{L}$ within the same coherence order. In other words, $\mathcal{L}$ is block-diagonal with respect to p^S in its matrix representation.

Many coherence pathways, characterized by the values p^S, can occur between successive pulses and then contribute to the net signal measured in a 2D-ELDOR experiment. However, information about the motional dynamics is adequately captured by just two of these coherence pathways, namely, S_{c+} and S_{c-}.[4,14,15,29] Taken together, they form the hypercomplex 2D-ELDOR signal. However, the S_{c-} pathway is echo-like, whereas the S_{c+} is free-induction decay (FID)-like (cf. Fig. 1). As a result, the S_{c+} signal decays faster under the effects of the inhomogeneous broadening canceled out in the S_{c-} signal. For very slow motions considered in this work, the S_{c+} signal emerging after the spectrometer dead time is greatly reduced compared to the S_{c-} signal. Therefore, in this paper, we focus on the S_{c-} coherence pathway.

The 2D-ELDOR S_{c-} coherence pathway proceeds as follows: initially, the electron spins are in the longitudinal coherence ($p^S = 0$). The first $\frac{\pi}{2}$ pulse takes them to the coherence order $p^S = +1$. For a time t_1, they remain in $p^S = +1$, and then a $\frac{\pi}{2}$ pulse transforms them to $p^S = 0$, where they are "stored" along the negative z-axis. They remain for time T_{mix} in $p^S = 0$, after which they are transformed to $p^S = -1$ by the final $\frac{\pi}{2}$ pulse. Signal collection can be performed after the final $\frac{\pi}{2}$ pulse.

Hence, the S_{c-} signal is a function of t_1, T_{mix}, and t_2. However, 2D-ELDOR signals are generally represented by the frequency variables f_1 and f_2, where f_1 and f_2 are the Fourier conjugate to the time

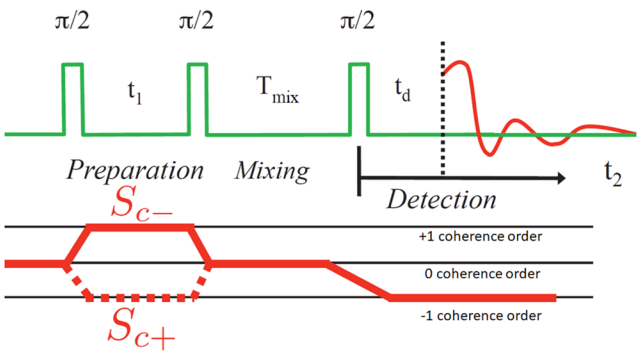

FIG. 1. A schematic of the 2D-ELDOR experiment, with three $\frac{\pi}{2}$-rotation microwave pulses. The coherence pathways S_{c+} and S_{c-} are also shown.

variables t_1 and t_2, respectively. Mathematically,

$$S_{c-}(f_1, T_{mix}, f_2) = \iint S_{c-}(t_1, T_{mix}, t_2) e^{2\pi i f_1 t_1} e^{-2\pi i f_2 t_2} dt_1 dt_2. \quad (2)$$

T_{mix} is fixed for a given 2D-ELDOR experiment. Note the receiver (or spectrometer) dead time t_d shown in the schematic. The 2D-ELDOR signal in the time interval t_d just after the final pulse is experimentally inaccessible.[14] Current state-of-the-art 2D-ELDOR experiments at 95 GHz ESR frequency have $t_d \sim 20$ ns.[14,51]

One of the great merits of the SLE is its applicability across a wide range of motional time scales, starting from the "rigid" limit, where the motion of the biomolecular structure carrying the electron spin label is too slow to be detected in an ESR experiment, to the motional narrowing regime, where anisotropic features of the spectrum are averaged out, leaving a collection of narrow, prominent hyperfine peaks, described by averaged g and A (hyperfine) values. 2D-ELDOR allows real-time detection of motions at time scales ranging from tens of nanoseconds to tens of microseconds. Changes in conformations of spin-labeled proteins, for example, do happen at such time scales.[30] However, such experiments usually require that the overall rotational diffusion of the protein be slower than conformational changes, so that effects from fluctuations in the structure of the protein can be clearly visible in the 2D-ELDOR spectrum. In the motional narrowing regime, these effects are not visible due to fast averaging over all orientations. Large proteins in the aqueous solvent typically have rotational diffusion constants $\sim 10^5$–10^6 s^{-1}, which corresponds to the very slow motional regime in ESR. Moreover, since higher ESR frequencies such as 95 GHz provide orientational resolution,[14] it is also important to perform these experiments at higher ESR frequencies, where the motions appear even slower on the ESR time scale.

There is thus a need to extend the computation of 2D-ELDOR spectra to higher frequencies and slower rotational diffusion rates, given the challenges noted in Sec. I. In Sec. III, we describe the original algorithm to compute 2D-ELDOR spectra and describe its limitations at high ESR frequencies, e.g., 95 GHz, and very slow motions. We then describe our new algorithm and show how it is more accurate for such slow rotational diffusion. In Sec. IV, we show how the new algorithm matches the rigid-limit 2D-ELDOR spectrum for extremely slow motions. In Sec. V, we consider a case of dynamic exchange of a protein domain between two conformations relative to the main protein structure and how the orientational resolution of the spectrum at 95 GHz enables one to infer details of the motion. Section VI provides the conclusions of our work.

III. IMPROVED ALGORITHM FOR COMPUTING 2D-ELDOR SPECTRA

A. Original algorithm for computing 2D-ELDOR spectra

The main task in computing the 2D-ELDOR spectrum is to track the orientation-dependent density matrix under the effect of the Liouville superoperator, $\mathcal{L}$. Moreover, in the absence of a microwave field, within a given coherence order p^S, $\mathcal{L}$ is time independent. This allows us to rewrite Eq. (1) in the following form:[29]

$$\frac{\partial \rho(\Omega, t)}{\partial t} = -\mathcal{L}_{(p^S)}(\rho(\Omega, t) - \rho_{eq}(\Omega)), \quad (3)$$

where $p^S \in \{0, +1, -1\}$. Equivalently,

$$\rho(\Omega, t) - \rho_{eq}(\Omega) = e^{-\mathcal{L}_{(p^S)}t}(\rho(\Omega, 0) - \rho_{eq}(\Omega)). \quad (4)$$

In the Liouville space, one represents ρ as a vector instead of a matrix, thus allowing us to represent $\mathcal{L}_{p^S}$ as a linear transformation on the entries of ρ stretched out in a column format. The matrix representation of $\mathcal{L}_{p^S}$, under appropriate symmetry transformations, becomes complex symmetric.[29] Synthesizing the expressions above, we can write the 2D-ELDOR signal (receiver dead time t_d assumed to be 0 for simplicity) as follows:

$$S_{c-}(t_1, T_{mix}, t_2) \propto \langle v_0 | e^{-\mathcal{L}_{-1}t_2} P_{-1\leftarrow 0} e^{-\mathcal{L}_0 T_{mix}} P_{0\leftarrow +1} e^{-\mathcal{L}_{+1}t_1} | v_0 \rangle. \quad (5)$$

Here $v_0 := (\rho(\Omega, t = 0^+) - \rho_{eq}(\Omega))$ denotes the initial density matrix in the $p^S = +1$ coherence right after the first $\frac{\pi}{2}$ microwave pulse, $P_{a\leftarrow b}$ is the linear transformation from $p^S = b$ to $p^S = a$ denoting the effect of the $\frac{\pi}{2}$ pulse, and $|\rangle$, $\langle|$ denote the usual bra–ket notation for a vector and its conjugate transpose.

Now, according to the description above, we must compute the effect of matrix exponentials $e^{-\mathcal{L}_{(p_S)}t}$ on vectors. By first calculating eigenvalues and eigenvectors, we can do this efficiently for any value of t. This forms the basis of the original algorithm.[29] The result of this algorithm is $S_{c-}(t_1, T_{mix}, t_2)$, and a double Fourier transform results in $S_{c-}(f_1, T_{mix}, f_2)$. Further details of the computational algorithm have been covered in earlier work.[14,23,24,29]

B. Limitations of the original algorithm

The above algorithm for 2D-ELDOR has been successfully applied for spectra involving faster rotational diffusion, i.e., $R \gtrsim 10^7$ s^{-1} (where R is the rotational tumbling rate), at ESR frequencies such as 9 GHz and 17 GHz.[29] For slower motions, especially for cases close to the rigid limit, this approach loses its accuracy in predicting reliable 2D-ELDOR spectra. The problem becomes more severe at higher ESR frequencies, e.g., 95 GHz. In Fig. B.1 of the supplementary material, we simulate a sample 2D-ELDOR spectrum at 95 GHz with $T_{mix} = 0$ ns and nuclear spin I = 1 (or equivalently, three hyperfine lines) and slow the rate of rotational diffusion, to see its effect on the computed 2D-ELDOR spectrum. We know that off-diagonal features such as cross-peaks should develop in a 2D-ELDOR spectrum only for non-zero mixing times T_{mix}, whereas these spectra show unexpected cross-peaks for $T_{mix} = 0$, indicating that we need higher computational accuracy for very slow rotational diffusion.

Moreover, as we slow down the motion further, we begin to see computed spectra that are significantly different from the expected ultra-slow-motional, rigid limit-like spectrum, as shown in Sec. IV. We now discuss the well-known causes behind such deviations from expected behavior.[23–28]

A crucial part of the original algorithm is to find eigenvalues and eigenvectors of the $\mathcal{L}_{(p^S)}$ matrices using the complex symmetric Lanczos tridiagonalization algorithm.[25,29] Round-off errors of the order of the machine precision can accumulate over Lanczos iterations, leading to a loss of orthogonality among successive Lanczos vectors.[24–26,52] This can result in unreliable eigenvalues and eigenvectors, rendering the computation of $e^{-\mathcal{L}_{(p^S)}t}|v\rangle$ inaccurate. It is important to observe here that the complex symmetric Lanczos algorithm is a variant of the Hermitian/real symmetric Lanczos

algorithm.[25,26,53] The complex symmetric version of Lanczos maintains orthogonality in a rectanormal sense, that is, $v_i^T v_j = 0$ for distinct Lanczos vectors v_i, v_j, whereas $v_i^\dagger v_j \neq 0$. Here the superscript T represents a vector's transpose, whereas † denotes its complex conjugate transpose. Figure 2 illustrates the loss of orthogonality in successive complex symmetric Lanczos iterations for nitroxide ESR spectra at 95 GHz. As the motion slows down, the non-normality of the SLE matrices increases, causing further Lanczos vectors to become even less orthogonal.

Past authors[23–26,29] have suggested several solutions to this problem, the major ones being reorthogonalization of Lanczos vectors and the use of quasi-minimum residual (QMR) to improve the convergence of Lanczos iterations, while maintaining the original goal of evaluating eigenvalues and eigenvectors. However, now we point out that there is a fundamental problem with these calculations for the complex symmetric SLE matrices as the motion becomes slower and the ESR frequency is greater. For such cases, the computation of eigenvalues and eigenvectors of $\mathcal{L}_{(p^s)}$ for slow rotational diffusion has an intrinsic numerical instability.[27,28]

Let us first revisit Eq. (1). The Liouville superoperator of Eq. (1) is non-normal, meaning that $\mathcal{L}\mathcal{L}^\dagger \neq \mathcal{L}^\dagger\mathcal{L}$. This crucial property renders the computation of 2D-ELDOR spectra to be challenging and markedly different from problems that enjoy Hermitian or real-symmetric structures. Another important consequence of $\mathcal{L}$ being non-self-adjoint, which has gained appreciation only in the past couple of decades,[27,28] is the ill-conditioning of the eigenvectors. Plainly put, it is possible for such non-normal matrices to find a scalar λ and a vector x such that $||Ax - \lambda x|| < \epsilon$, where ϵ is less than modern machine tolerances, and yet λ/x are far from being an actual eigenvalue/eigenvector. These effects grow in at much slower motions, making the use of eigenvectors/eigenvalues of $\mathcal{L}_{(p^s)}$ matrices at such motional rates susceptible to serious inaccuracies.[28] This issue cannot be resolved by the use of a different eigenvalue/eigenvector algorithm to compute slow-motional 2D-ELDOR spectra.

Therefore, a better approach is to compute 2D-ELDOR spectra without the use of eigenvalues and eigenvectors. In order to do so, we need to compute Eq. (5) in a way that avoids badly conditioned eigenvectors. One such approach, outlined in earlier work,[23] is to use conjugate gradients to solve the Ax = b problem for each new value of the magnetic field, i.e., x = x(B_0). This is the approach utilized in the past to "prune" the large set of basis vectors in cw ESR, thereby greatly reducing their size;[54] as pointed out in earlier work,[23] this is useful for computing cw ESR spectra when a broad range of B_0 is swept as for transition metal EPR spectra. However, since then, newer and more powerful algorithms have emerged to better deal with the serious complications of the non-normal properties of the SLE matrices for very slow motions. This is the subject of Subsection III C.

C. The improved algorithm

As we discussed earlier, we need to look at new ways to evaluate Eq. (5). An important observation to make here is that we plot the Fourier transform $S_{c-}(f_1, T_{mix}, f_2)$ of $S_{c-}(t_1, T_{mix}, t_2)$, which means

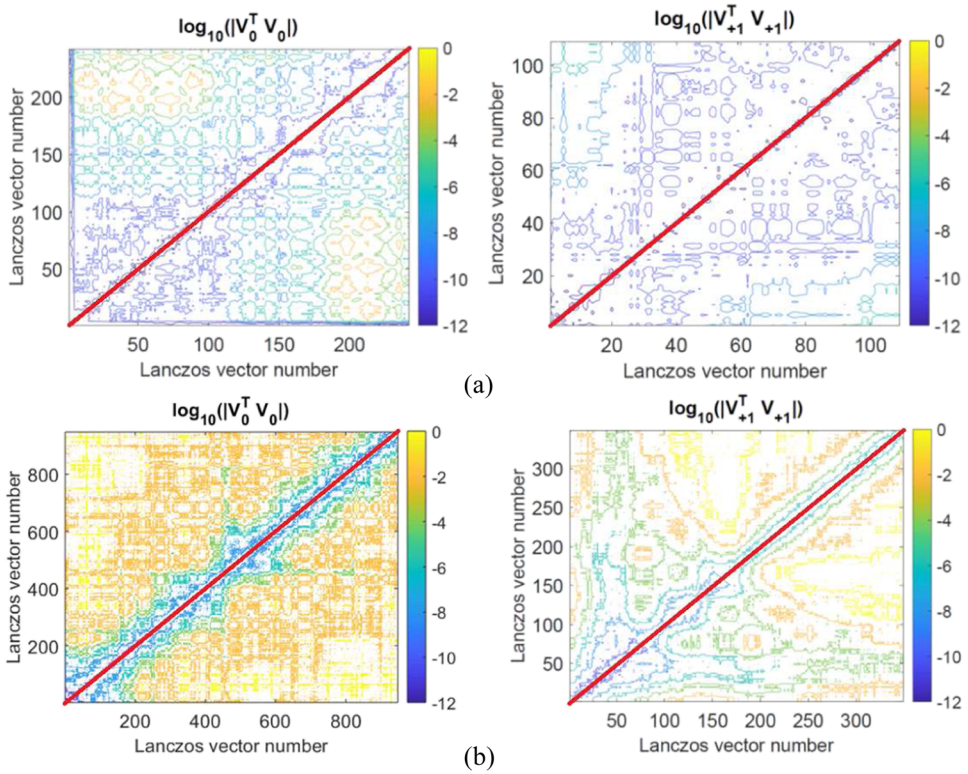

FIG. 2. Inner products of Lanczos vectors shown as a contour plot, for $\mathcal{L}_{(0)}$ and $\mathcal{L}_{(+1)}$. (a) Fast motions; (b) slow motions. Ideally, the inner product matrix of Lanczos vectors ($\langle \mathrm{IP} \rangle_{ij} = v_i^T v_j$) should be equal to the identity matrix. However, for slower motions, rather than going to 0, the inner products of further Lanczos vectors have values of the order of 10^{-2}, indicated by the yellow regions in the contour plot. The diagonal lines in these plots, where $i = j$ for Lanczos vectors, have been highlighted in red. The inner products along the diagonal, i.e., $v_i^T v_i = 1$, are due to normalization of Lanczos vectors to unity.

that we need to compute the double Fourier transform of

$$S_{c-}(t_1, T_{mix}, t_2).$$

However,

$$\begin{aligned}
&\iint S_{c-}(t_1, T_{mix}, t_2) e^{-2\pi i f_1 t_1} e^{2\pi i f_2 t_2} dt_1 dt_2 \\
&\quad \propto \iint \langle v_0 | e^{-\mathcal{L}_{-1} t_2} P_{-1\leftarrow 0} e^{-\mathcal{L}_0 T_{mix}} P_{0\leftarrow +1} e^{-\mathcal{L}_{+1} t_1} | v_0 \rangle e^{-2\pi i f_1 t_1} e^{2\pi i f_2 t_2} dt_1 dt_2 \\
&\quad = \iint \langle v_0 | e^{-\mathcal{L}_{-1} t_2} P_{-1\leftarrow 0} e^{-\mathcal{L}_0 T_{mix}} P_{0\leftarrow +1} e^{-\mathcal{L}_{+1} t_1} | v_0 \rangle e^{-2\pi i f_1 t_1} e^{2\pi i f_2 t_2} dt_1 dt_2 \\
&\quad = \langle v_0 | (\mathcal{L}_{-1} - 2\pi i f_2)^{-1} P_{-1\leftarrow 0} e^{-\mathcal{L}_0 T_{mix}} P_{0\leftarrow +1} (\mathcal{L}_{+1} + 2\pi i f_1)^{-1} | v_0 \rangle \\
&\quad = \langle z(f_2) | P_{-1\leftarrow 0} e^{-\mathcal{L}_0 T_{mix}} P_{0\leftarrow +1} | z(f_1) \rangle. \qquad (6)
\end{aligned}$$

Here, $|z(f)\rangle$ is defined as follows:

$$|z(f_1)\rangle = (\mathcal{L}_{+1} + 2\pi i f_1)^{-1} |v_0\rangle. \qquad (7)$$

In addition, as $\mathcal{L}_{-1} = \mathcal{L}_{+1}^{\dagger}$,

$$\langle v_0 | (\mathcal{L}_{-1} - 2\pi i f_2)^{-1} = \left((\mathcal{L}_{+1} + 2\pi i f_2)^{-1} | v_0 \rangle \right)^{\dagger} = \langle z(f_2) |. \qquad (8)$$

Therefore, in the left and right parts of the final expression in Eq. (6), namely, $\langle v_0 | (\mathcal{L}_{-1} + 2\pi i f_2)^{-1}$ and $(\mathcal{L}_{+1} + 2\pi i f_1)^{-1} | v_0 \rangle$, we need to compute only the effect of a matrix inverse on $|v_0\rangle$. This is a simpler problem than evaluating the matrix exponentials in Eq. (5) and can be recast as an Ax = b type linear equation problem. Furthermore, it does not suffer from badly conditioned eigenvalues and eigenvectors. Also, given that the $\mathcal{L}_{(p^S)}$ matrices are sparse, there are many fast and accurate modern algorithms available to choose from Refs. 55 and 56. In our work, we utilize the UMFPACK software package,[55] which performs a sparse LU factorization of the off-diagonal space ($p^S = +1$) matrix in order to calculate $|z(f_1)\rangle = (\mathcal{L}_{+1} + 2\pi i f_1)^{-1} |v_0\rangle$, for various values of f_1 across the bandwidth of the ESR spectrum.[57] We store these values of $|z(f_1)\rangle$ for further use. Note that this storage of multiple $z(f_1)$ vectors differs from the "aggregated diagonal space starting vector" used in the previous algorithm.[29] The key differences, however, are the absence of eigenvalue and eigenvector calculations, and the fact that the vectors $|z(f_1)\rangle$ are a function of sweep frequency rather than evolution time t_1.

We must reiterate here the existence of a similar proposal as noted above,[23] where the authors proposed to use the complex symmetric conjugate gradient (CSCG) algorithm to evaluate the 2D-ELDOR spectrum. We chose to not use the CSCG algorithm in our present work because of its slower convergence. Moreover, seeding a previous solution $|z(f)\rangle$ as an initial guess to evaluate $|z(f)\rangle$ for a new value of f did not significantly improve convergence either. We speculate that appropriate preconditioning techniques could improve this. However, we observe that UMFPACK results in a high-quality convergence approaching the machine precision for the $p^S = \pm 1$ coherence subspace matrices that we consider, while taking advantage of the sparsity of the SLE matrices.

We must point out here that, despite the need for the new algorithm at very slow motions, the original 2D-ELDOR algorithm should be the preferred choice for slow motional calculations where the tumbling rate is $\gtrsim 10^7$ s^{-1} at 95 GHz. The original algorithm, wherein eigenvalues and eigenvectors are calculated as needed, is faster than the new algorithm because in the original algorithm one does not need to sweep the calculations across frequency.

In cases where the matrix dimension is too large, one might need to take advantage of faster, iterative solvers like GMRES[57–59] to evaluate $|z(f_1)\rangle$, while sacrificing some accuracy. While UMFPACK is a direct solver, GMRES is a Krylov subspace method like CSCG, yet relies on the Arnoldi iteration[53] rather than the Lanczos iteration. This means we need to subtract projections from all the previous vectors at each iteration of GMRES, rather than using the 3-term recurrence relation as in the CSCG algorithm. GMRES also replaces the rectanormal inner product $\langle v_i, v_j \rangle = v_i^T v_j$ with the Hermitian inner product $\langle v_i, v_j \rangle = v_i^{\dagger} v_j$. Despite this speed disadvantage, we notice that GMRES helps us quickly attain acceptable values ($\leq 10^{-7}$) of the relative residual $||b - Ax||/||b||$ when solving Ax = b, where A is $\mathcal{L}_{+1}$ and b is $|v_0\rangle$. The GMRES solver we use has a restart provision, which restarts the GMRES algorithm after a fixed number of iterations ($M_{restart}$) repeatedly, resulting in faster computation as we need to subtract projections from a maximum of only $M_{restart}$ previous Arnoldi vectors rather than all the previous Arnoldi vectors.

We now consider the $e^{-\mathcal{L}_0 T_{mix}}$ term in Eq. (6), which acts on $|z(f_1)\rangle = (\mathcal{L}_{+1} + 2\pi i f_1)^{-1} |v_0\rangle$, via the linear transformation $P_{0\leftarrow +1}$. So, for each value of f_1, we get a different vector $|v(f_1)\rangle = P_{0\leftarrow +1} |z(f_1)\rangle$ for which $e^{-\mathcal{L}_0 T_{mix}} |v(f_1)\rangle$ should be computed. Note that $|v(f_1)\rangle$ is in a higher dimensional subspace ($p^S = 0$) when compared to $|z(f_1)\rangle$ ($p^S = +1$).

In other words, we are interested in the action of $e^{-\mathcal{L}_0 T_{mix}}$ on a set of known vectors $\{|v(f_1)\rangle\}$ in the $p^S = 0$ subspace, rather than the matrix elements of $e^{-\mathcal{L}_0 T_{mix}}$ themselves. The original algorithm calculated the eigenvalues of $\mathcal{L}_0$. However, as we discussed earlier, the non-normality of SLE matrices causes this computation to be inaccurate. To avoid the computation of eigenvalues and eigenvectors, we now compute $e^{-\mathcal{L}_0 T_{mix}} |v(f_1)\rangle$ in a different way. Expokit[60] and expm-multiply[61] are two approaches that are suitable for this task. We use the Expokit software, given its speed and memory efficiency. Expokit is a Krylov subspace package for computing $e^{-At} v$ for vectors v and sparse matrices A. The goal is to approximate the bigger vector space, where A and v reside, with a smaller subspace, while not sacrificing the accuracy of $e^{-At} v$. The first step in Expokit is to perform an Arnoldi procedure on A. However, there is a crucial difference between this Arnoldi procedure and the complex symmetric Arnoldi procedure. This Arnoldi procedure works with the usual Hermitian inner product, $\langle v_i, v_j \rangle = v_i^{\dagger} v_j$, rather than the rectanormal inner product we used earlier, i.e., $\langle v_i, v_j \rangle = v_i^T v_j$. This algorithm is not prone to loss of orthogonalization, unlike the complex symmetric Lanczos/CSCG algorithms. However, the result is an upper Hessenberg matrix instead of a tridiagonal matrix, which is much smaller yet non-sparse. Given the smaller size, we then employ standard matrix exponential functions like *expm*[61] to evaluate the action of the exponential of this matrix.

Combining the above two procedures, we have the scheme illustrated in Fig. 3 for computing the 2D-ELDOR signal. It is important to note that the new algorithm, although more accurate, is computationally more expensive. In the original algorithm, we diagonalized the $\mathcal{L}_{(p^S)}$ matrices once and used the eigenvectors and eigenvalues for computing the 2D-ELDOR spectra. Here, for each

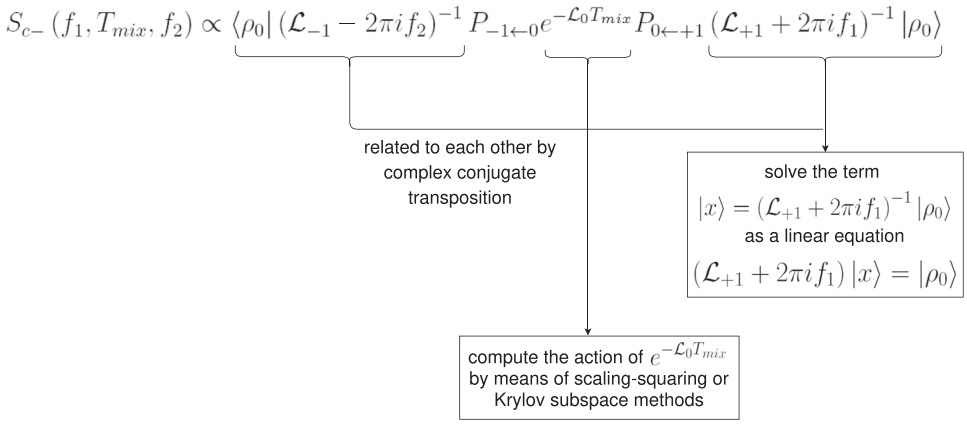

FIG. 3. Schematic for the new algorithm, which avoids computing eigenvalues and eigenvectors.

value of f_1, we need to compute $|v(f_1)\rangle$ and $e^{-\mathcal{L}_0 T_{mix}}|v(f_1)\rangle$. For the very slow motions of interest to us, however, the improvement in accuracy is immense. In other words, as noted above, for faster motions where the issues of non-normality are minor, the original algorithm is to be preferred because of its speed, but once the non-normality issues become important, it is necessary to employ the new algorithm.

In Sec. IV, we demonstrate the improved performance of the new algorithm when compared to the original algorithm.

IV. PERFORMANCE OF THE NEW ALGORITHM FOR ULTRA SLOW ROTATIONAL DIFFUSION

An important benchmark for an algorithm for computing slow-motional ESR spectra is whether it approaches the expected rigid limit spectrum when we make the rotational diffusion constants very small. The rigid limit spectrum [cf. Fig. 4(a)] is a powder average over all possible spin orientations and can be easily computed for the 2D-ELDOR case (see Sec. A of the supplementary material). The new algorithm, when applied for sufficiently slow rotational diffusion, yields the expected rigid limit spectrum [cf. Fig. 4(b)], whereas the original algorithm based on eigenvalues and eigenvectors predicts a spectrum much different from the expected spectrum [cf. Fig. 4(c)], demonstrating the concerns of Sec. III.

We must bear in mind that in order to achieve a perfect match with the rigid limit spectrum, we might have to go to even slower motions than the ones we consider here. Since the basis size grows sharply[29] when we slow down the rotational diffusion, we need ever larger matrices, thus making it difficult to compute 95 GHz 2D-ELDOR spectra for rotational diffusion slower than $R = 10^5\ \mathrm{s}^{-1}$. Thus, there is an almost undetectable difference, likely due to residual motional effects, between the computed spectrum and the rigid limit spectrum.

V. APPLICATION TO DYNAMIC EXCHANGE BETWEEN PROTEIN CONFORMATIONS

2D-ELDOR at slow motions and high microwave frequencies helps us in extending the reach of ESR from traditionally faster time scales to microsecond scale processes that can be observed in real time. Among these prospective applications, we focus here on conformational exchange occurring in proteins. Dynamic exchange between various protein conformations is crucial for protein function,[62] and such studies involve slow rotational diffusion. Also, fast rotational diffusion results in rotational averaging, making it challenging to discern effects like jumps between protein conformations. Slow-motional, high-frequency 2D-ELDOR, on the other hand, results in broad-bandwidth spectra due to incomplete rotational averaging, with different regions of the spectrum corresponding to different spin orientations.

Conformational exchange processes typically involve a dynamic equilibrium between two exchanging species A and B, each of which has a different conformation and a fixed mole fraction at equilibrium. Let c_A and c_B denote the fractions of molecules in conformations A and B, and we assume $c_A + c_B = 1$. The following equations describe the co-evolution of the density matrices of A and B:

$$\begin{aligned} \frac{\partial \rho_A}{\partial t} &= -\mathcal{L}_A^{(p^S)} \rho_A - k_{A\to B}\rho_A + k_{B\to A}\rho_B, \\ \frac{\partial \rho_B}{\partial t} &= -\mathcal{L}_B^{(p^S)} \rho_B + k_{A\to B}\rho_A - k_{B\to A}\rho_B. \end{aligned} \tag{9}$$

Here, $\mathcal{L}_A^{(p^S)}$, $\mathcal{L}_B^{(p^S)}$ denote the respective Liouville superoperators for conformations A and B, whereas $k_{A\to B}$ and $k_{B\to A}$ denote the forward and reverse rates of dynamic exchange between A and B. In this work, we assume that dynamic exchange otherwise preserves the rotational and spin states, i.e., their quantum numbers are preserved. While we acknowledge the possibility of using more refined models of dynamic exchange, we consider this model to be appropriate for the present work, given its simplicity, and to illustrate 2D-ELDOR spectra involving dynamic exchange.

Equation (9) can be written in the following convenient form:

$$\begin{bmatrix} \frac{\partial \rho_A}{\partial t} \\ \frac{\partial \rho_B}{\partial t} \end{bmatrix} = -\begin{bmatrix} \mathcal{L}_A^{(p^S)} + k_{A\to B}\mathbb{I} & -k_{B\to A}\mathbb{I} \\ -k_{A\to B}\mathbb{I} & \mathcal{L}_B^{(p^S)} + k_{B\to A}\mathbb{I} \end{bmatrix} \begin{bmatrix} \rho_A \\ \rho_B \end{bmatrix}. \tag{10}$$

Moreover, due to equilibrium between A and B, we also have

$$k_{A\to B} c_A = k_{B\to A} c_B. \tag{11}$$

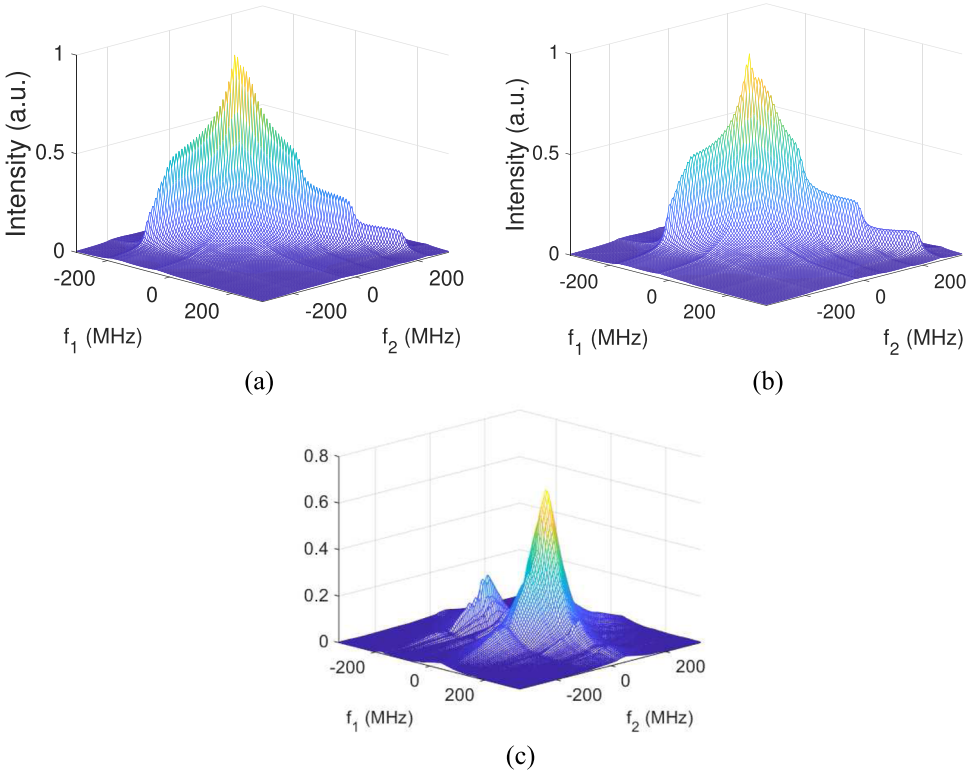

FIG. 4. Comparison of 95 GHz 2D-ELDOR spectra from the new and original algorithms at ultra-slow rotational diffusion with the expected rigid limit 2D-ELDOR spectrum, for a nitroxide spin label with nuclear spin $I = 1$, principal g tensor values (2.0087, 2.0057, 2.0021), principal A (hyperfine) tensor values (6, 6, 36) Gauss, at $T_{mix} = 0$ ns. Here $R_{\parallel}, R_{\perp}$ denote the principal values of the rotational diffusion tensor. (a) Rigid limit 2D-ELDOR spectrum, computed as in Sec. A of the supplementary material. (b) New algorithm, $R_{\parallel} = 10^5$, $R_{\perp} = 5 \times 10^4$ rad^2/s. (c) Same as (b), but with the original algorithm.

In order to maintain the complex symmetric structure of the 2 × 2 block Liouville superoperators in Eq. (10), we perform the following transformation, inspired by earlier work:[14,63]

$$\begin{bmatrix} \mathcal{L}_A^{(p^S)} + k_{A\to B}\mathbb{I} & -k_{sym}\mathbb{I} \\ -k_{sym}\mathbb{I} & \mathcal{L}_B^{(p^S)} + k_{B\to A}\mathbb{I} \end{bmatrix} = P_{eq}^{\frac{-1}{2}} \begin{bmatrix} \mathcal{L}_A^{(p^S)} + k_{A\to B}\mathbb{I} & -k_{B\to A}\mathbb{I} \\ -k_{A\to B}\mathbb{I} & \mathcal{L}_B^{(p^S)} + k_{B\to A}\mathbb{I} \end{bmatrix} P_{eq}^{\frac{1}{2}}, \tag{12}$$

where

$$P_{eq} = \begin{bmatrix} c_A & 0 \\ 0 & c_B \end{bmatrix}. \tag{13}$$

$k_{sym} = \sqrt{k_{A\to B}k_{B\to A}}$ denotes the mean exchange rate between A and B.

As a result of this transformation, the 2D-ELDOR signal can be rewritten as follows, in a way similar to Eq. (6):

$$\begin{aligned} &\iint S_{c-}(t_1, T_{mix}, t_2) e^{-2\pi i f_1 t_1} e^{2\pi i f_2 t_2} dt_1 dt_2 \\ &\propto \langle v_0 | (\mathcal{L}_{-1} + 2\pi i f_2)^{-1} P_{-1\leftarrow 0} e^{-\mathcal{L}_0 T_{mix}} P_{0\leftarrow +1} (\mathcal{L}_{+1} + 2\pi i f_1)^{-1} | P_{eq} v_0 \rangle \\ &= \langle v_0 P_{eq}^{\frac{1}{2}} | P_{eq}^{\frac{-1}{2}} (\mathcal{L}_{-1} + 2\pi i f_2)^{-1} P_{eq}^{\frac{1}{2}} P_{-1\leftarrow 0} P_{eq}^{\frac{-1}{2}} \\ &\quad \times e^{-\mathcal{L}_0 T_{mix}} P_{eq}^{\frac{1}{2}} P_{0\leftarrow +1} P_{eq}^{\frac{-1}{2}} (\mathcal{L}_{+1} + 2\pi i f_1)^{-1} P_{eq}^{\frac{1}{2}} | P_{eq}^{\frac{1}{2}} v_0 \rangle \\ &= \langle v_0 P_{eq}^{\frac{1}{2}} | \left(\widetilde{\mathcal{L}}_{-1} + 2\pi i f_2\right)^{-1} P_{-1\leftarrow 0} e^{-\widetilde{\mathcal{L}}_0 T_{mix}} P_{0\leftarrow +1} \left(\widetilde{\mathcal{L}}_{+1} + 2\pi i f_1\right)^{-1} | P_{eq}^{\frac{1}{2}} v_0 \rangle \\ &= \langle z(f_2) | P_{-1\leftarrow 0} e^{-\widetilde{\mathcal{L}}_0 T_{mix}} P_{0\leftarrow +1} | z(f_1) \rangle. \end{aligned} \tag{14}$$

Here,

$$v_0 = \begin{bmatrix} \rho_{0,A} \\ \rho_{0,B} \end{bmatrix}, \tag{15}$$

$$P_{0\leftarrow +1} = \begin{bmatrix} P_{0\leftarrow +1,A} & 0 \\ 0 & P_{0\leftarrow +1,B} \end{bmatrix}, \tag{16}$$

$$P_{-1\leftarrow 0} = \begin{bmatrix} P_{-1\leftarrow 0,A} & 0 \\ 0 & P_{-1\leftarrow 0,B} \end{bmatrix}, \tag{17}$$

$$\mathcal{L}_{p^S} = \begin{bmatrix} \mathcal{L}_A^{(p^S)} + k_{A\to B}\mathbb{I} & -k_{B\to A}\mathbb{I} \\ -k_{A\to B}\mathbb{I} & \mathcal{L}_B^{(p^S)} + k_{B\to A}\mathbb{I} \end{bmatrix}, \tag{18}$$

$$\widetilde{\mathcal{L}}_{p^S} = \begin{bmatrix} \mathcal{L}_A^{(p^S)} + k_{A\to B}\mathbb{I} & -k_{sym}\mathbb{I} \\ -k_{sym}\mathbb{I} & \mathcal{L}_B^{(p^S)} + k_{B\to A}\mathbb{I} \end{bmatrix}, \tag{19}$$

and

$$|z(f)\rangle = \left(\widetilde{\mathcal{L}}_{+1} + 2\pi i f_1\right)^{-1} | P_{eq}^{\frac{1}{2}} v_0 \rangle. \tag{20}$$

We apply the model described above to a spin-labeled protein with two domains. The first and main domain determines the principal axes of the rotational diffusion tensor, and the second much smaller domain, with a rigid spin label attached to it, jumps between two possible conformations with respect to the first domain. Each of the two conformations could be visualized as at a different diffusion tilt[64] (α_d, β_d, γ_d) of the g and A tensor frames with respect to the

frame formed by the principal axes of the rotational diffusion tensor. We assume that the orientations of the principal axes and principal values of the rotational diffusion tensor do not change during jumps by the second domain in going from conformation A to B. This approximation is valid as long as the bulk of the protein maintains its structure and has significantly higher rotational inertia when compared to the part of the protein that jumps. Moreover, g and A tensor frames are assumed to be coincident. To further simplify our treatment, we consider the conformations to have diffusion tilts of (0, 0, 0) and (0, β_d, 0), relative to the principal axes of the protein's diffusion tensor. Figure 5 depicts this exchange process between A and B. Experimentally, we could realize such a system by means of site-directed spin labeling using a rigid bidentate label.[30,31]

These calculations typically result in large, sparse matrices that are roughly 30 000 × 30 000 in size. However, not all initial basis vectors in the respective coherence subspaces (p^S = 0, +1, −1) are important. That is, some components of $|z(f)\rangle$ have insignificant magnitude. Without sacrificing accuracy, we can safely prune[54] out these basis vectors, thus resulting in much smaller matrices and much faster computations. In this work, we use the aforementioned pruning procedure and set the pruning tolerance[54] to 0.01. Details about the pruning tolerance and the pruning procedure can be found in earlier work.[23,54]

To check whether our pruning is excessive or not, we chose 20 frequency points in the cw spectrum and compared the cw spectra at those 20 frequency values before and after pruning. We find the root mean square (rms) deviation between the intensities of the cw spectra to be less than 0.2%, thus indicating our pruning is not excessive.

A. Development of dynamic exchange cross-peaks as a function of mixing time

Effects of exchange processes in 2D-ELDOR develop with mixing time T_{mix}. However, we must highlight here the crucial difference between 2D-ELDOR cross-peaks in the absence of exchange and the cross-peaks due to dynamic exchange. Individual 2D-ELDOR spectra from the two conformations look quite similar, and ultra-slow-motional spectra are broad and continuous. Each "dynamic spin packet"[65] (infinitesimal element of the spectrum) from conformation A exchanges with another dynamic spin packet from conformation B, and vice versa. Therefore, the cross-peaks, rather than being sharp, are broadened. Figure 6 shows this development of exchange cross-peaks as a function of mixing time. Nevertheless, they are clearly distinguishable from any "spectral diffusion cross-peaks"[29,65] due to the slow protein tumbling that simply appears as a broadening of all the auto-peaks in a direction orthogonal to the $f_1 = f_2$ diagonal also as a function of T_{mix}.[66] Here $\beta_d = 90°$ and involves motion of the exchanging domain between the conformation where the z magnetic tensor axis of the spin label is parallel to the z principal axis of the protein diffusion tensor and the one where the x magnetic tensor axis of the spin label is parallel to the z principal axis of the protein diffusion tensor. The results shown in Fig. 6 are reproduced in Fig. C.1 of the supplementary material, wherein the dominant auto-peaks have been removed. For T_{mix} = 0 ns, one just sees the residual edges of the auto-peaks that were not entirely removed. However, for T_{mix} > 0 ns, one clearly sees the exchange cross-peaks grow in.

B. Dependence of dynamic exchange on the jump angle, β_d

β_d denotes the jump angle between the conformations A and B. The smaller the value of β_d, the closer the dynamic spin packets that exchange with each other. This causes cross-peaks to be less visible, as they are closer to the auto-peaks. For larger values of β_d, however, the cross-peaks occur between dynamic spin packets with greater spectral separation, causing them to become more visible. That is, the cross-peaks occur between more separated orientations, and thus they show up prominently in locations well-separated from the $f_1 = f_2$ diagonal. For $\beta_d = 0°$, there are no exchange cross-peaks, as expected. Figure 7 shows the exchange spectra for $\beta_d = 0°$, $\beta_d = 45°$, and $\beta_d = 90°$ for motion in the x–z plane of the spin label's magnetic tensor relative to the protein's principal axis of diffusion; that is, $\beta_d = 0°$ corresponds to the z axis of the label's magnetic tensor parallel to the protein's z axis, whereas $\beta_d > 0°$ corresponds to a tilt of the label's x–z plane relative to the protein's z axis.

It is important to note that the individual 2D-ELDOR spectra from the two conformations look quite similar. However, the exchange term causes cross-peaks between one orientation of the spin label in conformation A with another orientation of the spin label in conformation B. Figure 7 is replotted in Fig. C.2 of the supplementary material with auto-peaks subtracted to better show the cross-peaks that develop.

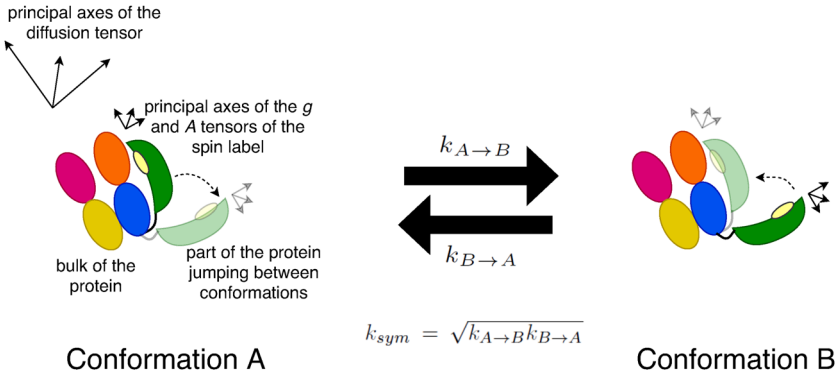

FIG. 5. Schematic showing dynamic exchange between two conformations. The rigid spin label, shown in light yellow, is attached to the part of the protein that jumps between two conformations A and B, which in turn is shown in green. The remaining parts of the protein represent its bulk, which is unaffected during conformational changes.

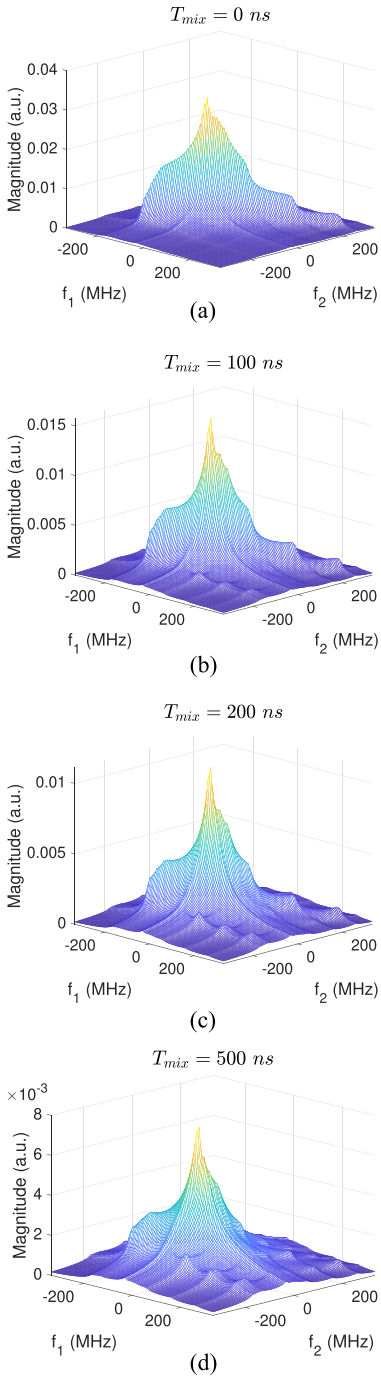

FIG. 6. Effect of dynamic exchange on slow-motional 2D-ELDOR spectra, as a function of mixing time. Here $k_{sym} = 10^6\ s^{-1}$, $R_{\parallel} = 10^5\ s^{-1}$, and $R_{\perp} = 5 \times 10^4\ s^{-1}$. Both conformations have the same mole fraction, i.e., $c_A = c_B = 0.5$. (a) $T_{mix} = 0$ ns, (b) $T_{mix} = 100$ ns, (c) $T_{mix} = 200$ ns, and (d) $T_{mix} = 500$ ns. Other parameters are the same as Fig. 4. Note that the amplitude of the signal decreases with mixing time, T_{mix}, as the cross-peak development spreads the 2D signal out. However, the integrated intensity remains constant as we have not included any T_1 decay. In Fig. C.1 of the supplementary material, we show the same spectra after removing the dominant auto-peaks, in order to better highlight the cross-peaks.

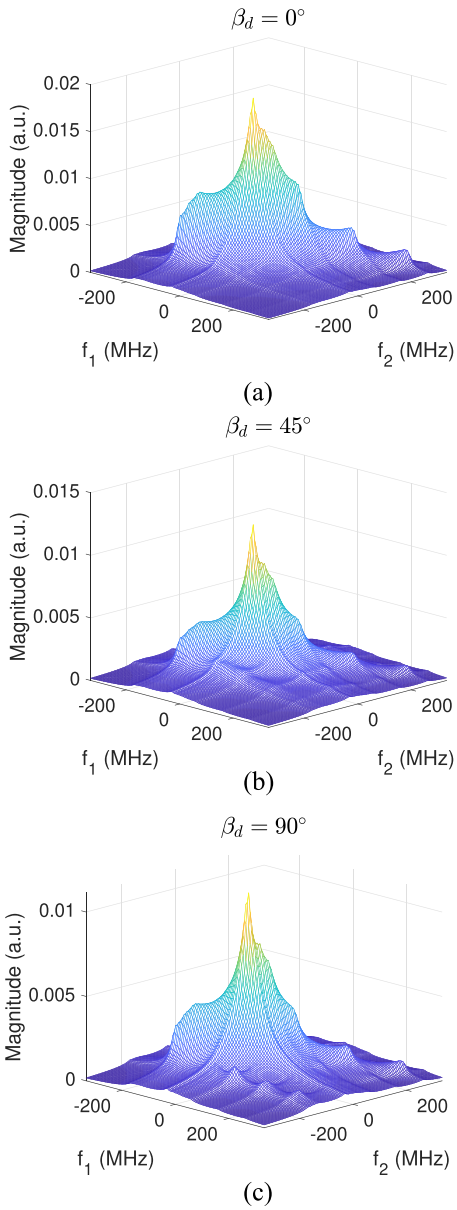

FIG. 7. Effect of dynamic exchange on slow-motional 2D-ELDOR spectra, as a function of β_d: (a) $\beta_d = 0°$, (b) $\beta_d = 45°$, and (c) $\beta_d = 90°$. Here $T_{mix} = 200$ ns, $k_{sym} = 10^6\ s^{-1}$, and $c_A = c_B = 0.5$. Other parameters are the same as Fig. 6. In Fig. C.2 of the supplementary material, we show the same spectra after auto-peak subtraction, in order to better highlight the cross-peaks.

What is of considerable physical significance is that, given the orientational resolution, one can "read off" the nature of the motion directly from the 2D spectrum. This is shown in Fig. 8, which is a contour plot of Fig 7(c) with the intense auto-peaks removed to better focus on the exchange cross-peaks. The 1D projections at the left side and bottom of the contour plot show the derivative of the

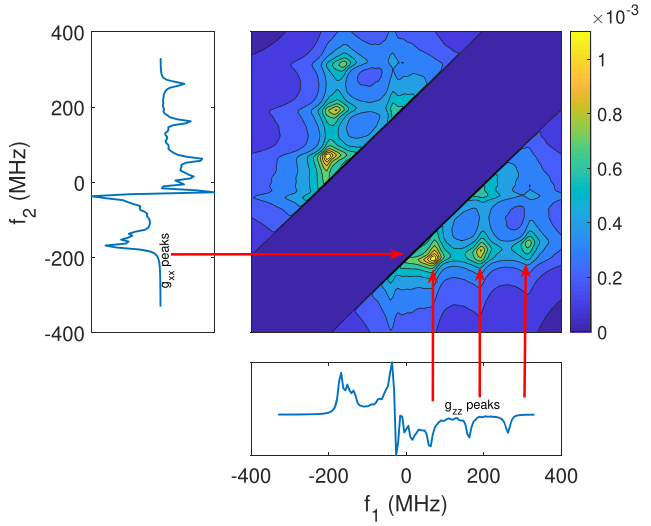

FIG. 8. 95 GHz exchange spectrum (with auto-peak subtraction to better show exchange cross-peaks), showing cross-peaks generated for motion between g_{xx} and g_{zz} regions of the cw ESR spectrum. The plots to the left and bottom of the contour plot show the spectra obtained by taking the derivative of the sum of the real part of the signal $S_{c-}(f_1, f_2)$ over either f_1 or f_2. Notice the similarity of the two aforementioned plots to the rigid limit cw spectrum.[67] The diagonal in this figure has been rotated 45° in the f_1–f_2 plane from that in Fig. 7 for purposes of clarity in presentation.

summed spectra wherein the g_{xx}, g_{yy}, and g_{zz} regions are clearly discerned as is the case for cw 95 GHz nitroxide spectra near the rigid limit.[67] The red arrows point to the cross-peaks generated by the jump motion showing clearly it is between the x and z spin magnetic axes.

In Fig. 9(a), we show the 2D spectrum when the jump motion interchanges the y and z axes with $\beta_d = 90°$, where exchange cross-peaks are evident. In Fig. 9(b), this is shown in a contour plot analogous to that of Fig. 8. Here the cross-peaks show the motion to be in the y–z magnetic plane of the spin label.

C. Dependence of dynamic exchange on k_{sym}

Figure 10 shows these dynamic exchange cross-peaks for different values of k_{sym}. In the absence of dynamic exchange ($k_{sym} = 0$), of course we do not see any exchange cross-peaks, whereas in the presence of dynamic exchange ($k_{sym} \neq 0$), we see cross-peaks between various spin orientations. For faster dynamic exchange, the cross-peaks at a given mixing time (T_{mix}) are more intense. These results are shown with the auto-peaks removed in Fig. C.3 of the supplementary material to emphasize the cross-peaks.

D. Dependence of dynamic exchange on the ESR frequency

At lower ESR frequencies, the exchange cross-peaks lack the orientational resolution available at 95 GHz. Figure 11 shows the dependence of exchange 2D-ELDOR spectra on the ESR frequency

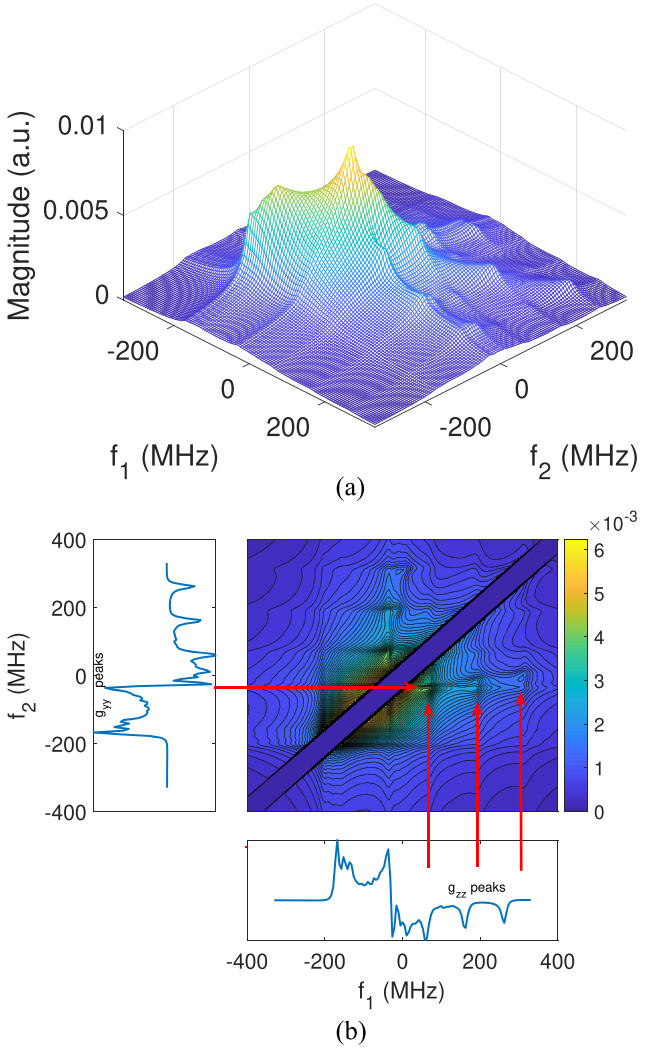

FIG. 9. (a) 95 GHz exchange spectrum, showing cross-peaks generated for motion between g_{yy} and g_{zz} regions of the cw ESR spectrum. In (b), the line plots to the left and bottom of the contour plot show the spectra obtained by taking the derivative of the sum of the real part of the signal $S_{c-}(f_1, f_2)$ over either f_1 or f_2, as in Fig. 8. Here T_{mix} = 200 ns, $c_A = c_B = 0.5$, $k_{sym} = 10^6$ s^{-1}, and jump angle $\beta_d = 90°$. Other parameters are the same as Fig. 6.

for 9 GHz, 17 GHz, 35 GHz, and 95 GHz, and Fig. C.4 of the supplementary material shows these results with the auto-peaks removed. At 9 GHz, for example, the x, y, and part of the z orientation of the spin label are bunched in the spectral center, although outer peaks do refer to the remainder of the contribution of the z orientation. The latter do show cross-peaks with the central region, but it is not possible to determine with which of the orientations, since they are bunched in the spectral center. Similar comments apply to the 17 GHz case, whereas 35 GHz represents the worst case, since the competing contributions from hyperfine and g-tensor terms are comparable.

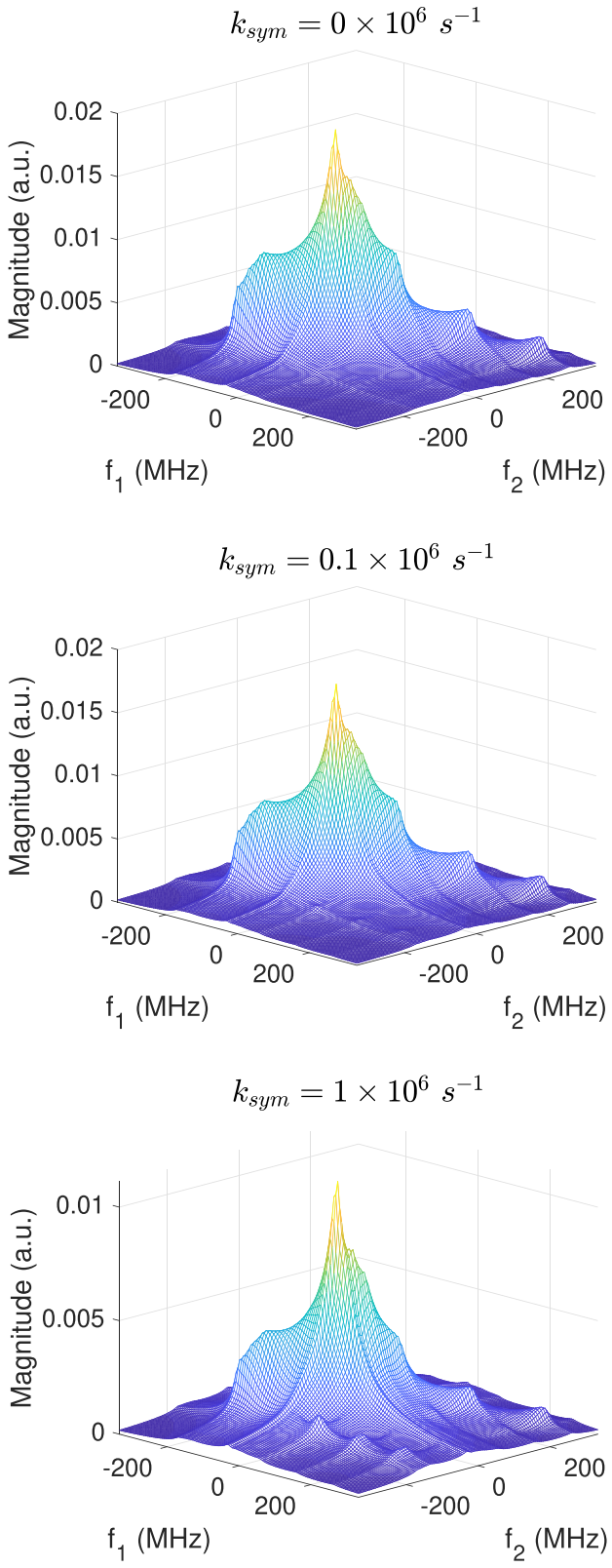

FIG. 10. Effect of k_{sym} on slow-motional 2D-ELDOR spectra: (a) k_{sym} = 0 s^{-1} (no exchange), (b) k_{sym} = 10^5 s^{-1}, and (c) k_{sym} = 10^6 s^{-1}. Here T_{mix} = 200 ns, jump angle β_d = 90°, and c_A = c_B = 0.5. Other parameters are the same as Fig. 6. In Fig. C.3 of the supplementary material, we show the same spectra again after auto-peak subtraction, in order to better highlight the cross-peaks. For example, cross-peaks for k_{sym} = 0.1 × 10^6 s^{-1} become more pronounced after this subtraction procedure.

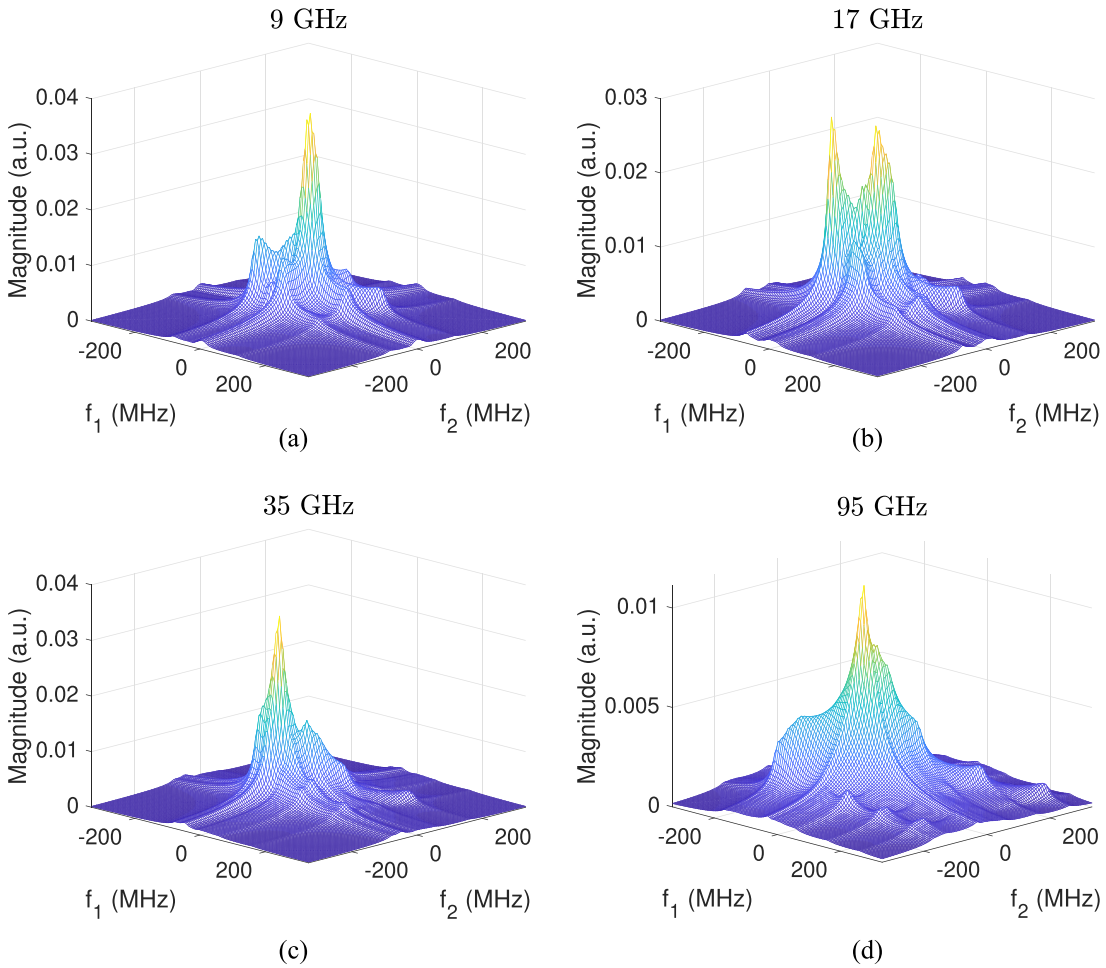

FIG. 11. Effect of ESR frequency on slow-motional 2D-ELDOR spectra: (a) 9 GHz, (b) 17 GHz, (c) 35 GHz, and (d) 95 GHz. Here T_{mix} = 200 ns, $c_A = c_B = 0.5$, $k_{sym} = 10^6$ s^{-1}, and jump angle $\beta_d = 90°$. Other parameters are the same as Fig. 6. In Fig. C.4 of the supplementary material, we show the same spectra after auto-peak subtraction, in order to better highlight the cross-peaks.

VI. CONCLUSION AND OUTLOOK

In this work, we describe a significant improvement over the original algorithm for simulating high frequency, slow-motional 2D-ELDOR spectra. Our new algorithm avoids calculating the numerically sensitive eigenvalues and eigenvectors of the stochastic Liouville equation matrices $\mathcal{L}_{(p^S)}$ used for computing the 2D-ELDOR signal. With this approach, we are now successful in matching our computed ultra-slow-motional 2D-ELDOR spectra with the expected rigid limit (powder averaged) 2D-ELDOR spectrum. The essentials of our new algorithm extend to all forms of two-dimensional ESR spectroscopies and can readily address experiments involving more complicated microwave pulse sequences. Predictions from our new algorithm can guide novel multi-dimensional ESR studies of biomolecules such as proteins and lipids at slow motions, giving one an opportunity to take full advantage of greater orientational resolution at higher ESR frequencies due to incomplete motional averaging of spectra. Moreover, given the versatility of 2D-ELDOR in terms of the mixing time (T_{mix}) dimension, we can extend the range of ESR to cover nanoseconds to microseconds in real time. In particular, one can study dynamic exchange processes between conformations of a spin-labeled protein occurring at the aforementioned time scales. Our work is timely, in the sense that there have been concurrent developments in performing 2D-ELDOR experiments at the high microwave frequency of 95 GHz with low receiver dead times (~20 ns).[51] We also demonstrate in this work some examples of model 2D-ELDOR spectra involving a simple dynamical exchange between two conformations of a spin-labeled domain in a protein, each of which corresponds to a different set of diffusion tilt angles between the principal axes of rotational diffusion of the protein and that of the *g* and *A* tensors in the smaller domain. A key prediction is the presence of well-defined exchange cross-peaks in 95 GHz 2D-ELDOR spectra where the protein is undergoing very slow rotational diffusion.

Further improvements to this work would include integrating an automated non-linear least squares procedure[64] to fit 2D-ELDOR spectra in terms of parameters such as rotational diffusion and dynamic exchange rate. Depending on the spin-labeled protein studied experimentally, one might need to fine-tune the model of dynamic exchange appropriately and possibly modify the SLE matrices. Nevertheless, we look forward to applications of this work for extending the scope of 2D-ELDOR in order to study biophysical processes that occur over sub-microsecond time scales.

SUPPLEMENTARY MATERIAL

The supplementary material consists of details regarding how we calculate the rigid limit 2D-ELDOR S_{c-} intensity and the presence of unexpected 2D-ELDOR cross-peaks at very slow motional rates when using the original 2D-ELDOR simulation algorithm. Additionally, we again show figures from the main text, with the auto-peaks removed in order to better demonstrate the exchange cross-peaks.

ACKNOWLEDGMENTS

This work was supported by the National Institute of General Medical Sciences (NIGMS), Grant No. P41GM103521 (NIGMS/NIH). In addition, the authors acknowledge the inputs of David Schneider, Brian Crane, Boris Dzikovski, Curt Dunnam, Siddarth Chandrasekaran, Timothee Chauvire, and members of the Cornell Center for Advanced Computing.

DATA AVAILABILITY

The data and computer programs that support the findings of this study are available from the corresponding author upon reasonable request.

REFERENCES

[1] P. Borbat, A. Costa-Filho, K. Earle, J. Moscicki, and J. H. Freed, Science **77**, 3915 (2001).
[2] P. Borbat and J. H. Freed, in *EPR Spectroscopy: Fundamentals and Methods*, edited by D. Goldfarb and S. Stoll (Wiley and Sons, 2018), Chap. 11, pp. 401–424.
[3] J. H. Freed, in *Biological EPR, Part B: Methodology, Instrumentation, and Dynamics*, Biological Magnetic Resonance Vol. 24/B, edited by S. Eaton, G. Eaton, and L. Berliner (Springer, NY, 2005), Chap. 9.
[4] S. Misra and J. H. Freed, in *Multifrequency Electron Paramagnetic Resonance*, edited by S. Misra (Wiley-VCH Verlag GmbH & Co. KGaA, 2011), pp. 497–544.
[5] P. Borbat and J. H. Freed, in *Structural Information from Spin-Labels and Intrinsic Paramagnetic Centres in the Biosciences*, Structure and Bonding Vol. 152, edited by C. Timmel and J. R. Harmer (Springer, Berlin, Heidelberg, 2013), pp. 1–82.
[6] W. L. Hubbell, C. J. López, C. Altenbach, and Z. Yang, Curr. Opin. Struct. Biol. **23**, 725 (2013).
[7] A. Polimeno, V. Barone, and J. H. Freed, in *Computational Strategies for Spectroscopy*, edited by V. Barone (Wiley, NY, 2012), pp. 549–582.
[8] G. Jeschke, Prog. Nucl. Magn. Reson. Spectrosc. **72**, 42 (2013).
[9] Z. Zhang, M. R. Fleissner, D. S. Tipikin, Z. Liang, J. K. Moscicki, K. A. Earle, W. L. Hubbell, and J. H. Freed, J. Phys. Chem. B **114**, 5503 (2010).
[10] W. B. Lynch, K. A. Earle, and J. H. Freed, Rev. Sci. Instrum. **59**, 1345–1351 (1988).
[11] K. A. Earle, J. K. Moscicki, A. Polimeno, and J. H. Freed, J. Chem. Phys. **106**, 9996 (1997).
[12] J. H. Freed, in *Very High Frequency ESR*, edited by O. Y. Grinberg and L. J. Berliner (Springer, New York, 2004), Chap. 2.
[13] D. Sezer, J. H. Freed, and B. Roux, J. Am. Chem. Soc. **131**, 2597 (2009).
[14] J. M. Franck, S. Chandrasekaran, B. Dzikovski, C. R. Dunnam, and J. H. Freed, J. Chem. Phys. **142**, 212302 (2015).
[15] S. Lee, B. R. Patyal, S. Saxena, R. H. Crepeau, and J. H. Freed, Chem. Phys. Lett. **221**, 397 (1994).
[16] D. Xu, R. H. Crepeau, C. K. Ober, and J. H. Freed, J. Phys. Chem. **100**, 15873 (1996).
[17] V. S. S. Sastry, A. Polimeno, R. H. Crepeau, and J. H. Freed, J. Chem. Phys. **105**, 5753 (1996).
[18] A. J. Costa-Filho, Y. Shimoyama, and J. H. Freed, Biophys. J. **84**, 2619 (2003).
[19] Y.-W. Chiang, A. J. Costa-Filho, and J. H. Freed, J. Phys. Chem. B **111**, 11260 (2007).
[20] W. Hofbauer, K. A. Earle, C. R. Dunnam, J. K. Moscicki, and J. H. Freed, Rev. Sci. Instrum. **75**, 1194 (2004).
[21] K. A. Earle, B. Dzikovski, W. Hofbauer, J. K. Moscicki, and J. H. Freed, Magn. Reson. Chem. **43**, S256–S266 (2005).
[22] P. A. S. Cruickshank, D. R. Bolton, D. A. Robertson, R. I. Hunter, R. J. Wylde, and G. M. Smith, Rev. Sci. Instrum. **80**, 103102 (2009).
[23] D. Schneider and J. H. Freed, *Lasers, Molecules and Methods*, edited by C. Hirschfelder and R. E. Wyatt (McGraw-Hill, 1989), Chap. 10, p. 431.
[24] Y.-W. Chiang and J. H. Freed, J. Chem. Phys. **134**, 034112 (2011).
[25] G. Moro and J. H. Freed, J. Chem. Phys. **75**, 3157 (1981).
[26] J. K. Cullum and R. A. Willoughby, *Lanczos Algorithms for Large Symmetric Eigenvalue Computations* (Birkhauser, Boston, 1985).
[27] L. Trefethen and M. Embree, *Spectra and Pseudospectra* (Princeton University Press, 2005).
[28] D. Schneider, "Spectral decompositions and slow motional lineshape analysis," in Rocky Mountain Conference on Analytical Chemistry, 2004.
[29] S. Lee, D. E. Budil, and J. H. Freed, J. Chem. Phys. **101**, 5529 (1994).
[30] C. Altenbach, A. K. Kusnetzow, O. P. Ernst, K. P. Hofmann, and W. L. Hubbell, Proc. Natl. Acad. Sci. U. S. A. **105**, 7439 (2008).
[31] S.-Y. Park, P. P. Borbat, G. Gonzalez-Bonet, J. Bhatnagar, A. M. Pollard, J. H. Freed, A. M. Bilwes, and B. R. Crane, Nat. Chem. Struct. Biol. **13**(5), 400 (2009).
[32] D. D. Boehr, D. McElheny, H. J. Dyson, and P. E. Wright, Science **313**(5793), 1638 (2006).
[33] D. K. Chakravorty and K. M. Merz, Acc. Chem. Res. **48**(2), 439 (2015).
[34] C. Kandt and L. Monticelli, in *Membrane Protein Structure Determination: Methods and Protocols*, edited by J. J. Lacapere (2010), Vol. 654, pp. 423–440.
[35] G. L. Sala, S. Decherchi, M. D. Vivo, and W. Rocchia, ACS Central Science **3**(9), 949 (2017).
[36] M. K. Rout, C. D. Hodge, C. J. Markin, X. Xu, J. N. M. Glover, W. Xiao, and L. Spyracopoulos, J. Am. Chem. Soc. **136**(50), 17446 (2014).
[37] M. Gabba, S. Poblete, T. Rosenkranz, A. Katranidis, D. Kempe, T. Züchner, R. G. Winkler, G. Gompper, and J. Fitter, Biophys. J. **107**(8), 1913 (2014).
[38] A. Pabis, V. A. Risso, J. M. Sanchez-Ruiz, and S. C. Kamerlin, Curr. Opin. Struct. Biol. **48**, 83 (2018).
[39] Y. Wang, K. Bugge, B. B. Kragelund, and K. Lindorff-Larsen, Curr. Opin. Struct. Biol. **48**, 74 (2018).
[40] Y. Lee, R. Lazim, S. J. Y. Macalino, and S. Choi, Curr. Opin. Struct. Biol. **55**, 147 (2019).
[41] A. Chandran, X. Chee, D. L. Prole, and T. Rahman, Sci. Rep. **9**, 2454 (2019).
[42] L.-T. Da and M. Lin, Phys. Chem. Chem. Phys. **21**(47), 26003 (2019).
[43] S. Dutta, S. Kundu, A. Saha, and N. Nandi, J. Biomol. Struct. Dyn. **36**(4), 878 (2018).
[44] N. B. Guros, A. Balijepalli, and J. B. Klauda, Proc. Natl. Acad. Sci. U. S. A. **117**(1), 405 (2020).

[45]A. J. W. Hartel, P. Ong, I. Schroeder, M. H. Giese, S. Shekar, O. B. Clarke, R. Zalk, A. R. Marks, W. A. Hendrickson, and K. L. Shepard, Proc. Natl. Acad. Sci. U. S. A. **115**(8), E1789 (2018).
[46]T. Lei, Z. Hu, R. Ding, J. Chen, S. Li, F. Zhang, X. Pu, and N. Zhao, ACS Chem. Neurosci. **11**(2), 133 (2020).
[47]R. Nygaard, Y. Zou, R. O. Dror, T. J. Mildorf, D. H. Arlow, A. Manglik, A. C. Pan, C. W. Liu, J. J. Fung, M. P. Bokoch, F. S. Thian, T. S. Kobilka, D. E. Shaw, L. Mueller, R. S. Prosser, and B. K. Kobilka, Cell **152**(3), 532 (2013).
[48]D. Samanta, P. P. Borbat, B. Dzikovski, J. H. Freed, and B. R. Crane, Proc. Natl. Acad. Sci. U. S. A. **112**(8), 2455 (2015).
[49]S. Wiesner, L. E. Wybenga-Groot, N. Warner, H. Lin, T. Pawson, J. D. Forman-Kay, and F. Sicheri, EMBO J. **25**(19), 4686 (2006).
[50]J. H. Freed, G. V. Bruno, and C. Polnaszek, J. Chem. Phys. **55**, 5270 (1971).
[51]C. Dunnam, B. Dzikovski, J. Franck, and J. H. Freed, "ACERT 95 GHz MKII ESR spectrometer," in 21st International Society of Magnetic Resonance Conference, Berlin, Germany, 2019.
[52]I. Kuprov, J. Magn. Reson. **195**, 45 (2008).
[53]G. H. Golub and C. V. Loan, *Matrix Computations* (Johns Hopkins University Press, 2013), Chap. 11, pp. 597–680.
[54]K. V. Vasavada, D. J. Schneider, and J. H. Freed, J. Chem. Phys. **86**(2), 647 (1987).
[55]T. A. Davis, ACM Trans. Math. Software **30**, 196 (2004).
[56]O. Schenk and K. Gaertner, Future Gener. Comput. Syst. **20**, 475 (2004).
[57]A referee has pointed out that UMFPACK and GMRES are utilized in EasySpin [S. Stoll and A. Schweiger, J. Magn. Reson. **178**(1), 42 (2006)] and Spinach [I. Kuprov, *ibid* **208**, 179 (2011); **270**, 124 (2016)].
[58]Y. Saad and M. H. Schultz, SIAM J. Sci. Stat. Comput. **7**(3), 856 (1986).
[59]R. Barrett, M. Berry, and T. F. Chan, *Templates for the Solution of Linear Systems: Building Blocks for Iterative Methods* (SIAM, 1994), Chap. 10, pp. 218–230.
[60]R. B. Sidje, ACM Trans. Math. Software **24**(1), 130 (1998).
[61]A. H. Al-Mohy and N. J. Higham, SIAM J. Sci. Comput. **33**(2), 488 (2011).
[62]D. D. Boehr, R. Nussinov, and P. E. Wright, Nat. Chem. Biol. **5**, 789 (2009).
[63]E. Meirovitch, D. Igner, E. Igner, G. Moro, and J. H. Freed, J. Phys. Chem. **77**, 3915 (1982).
[64]D. E. Budil, S. Lee, S. Saxena, and J. H. Freed, J. Magn. Reson. A **120**, 155 (1996).
[65]S. Saxena and J. H. Freed, J. Phys. Chem. A **101**, 7998 (1997).
[66]We note that in Fig. 6 and all subsequent figures we have not added any T_1 (i.e., electron-spin flip terms) for simplicity. This is not an important matter in this study as typical T_1's at 95 GHz are on the order of 1–2 μs [B. Dzikovski, private communication (2020)] and at 17 GHz on the order of 3–10 μs [P. Borbat, private communication (2020)].
[67]B. Dzikovski, D. Tipikin, and J. Freed, J. Phys. Chem. B **116**, 6694 (2012).